

The role of photospheric converging motion in initiation of solar eruptions

Xinkai Bian¹, Chaowei Jiang¹ and Xueshang Feng¹

¹*Institute of Space Science and Applied Technology, Harbin Institute of Technology, Shenzhen 518055, China*

Correspondence*:
Chaowei Jiang
chaowei@hit.edu.cn

ABSTRACT

It is well known that major solar eruptions are often produced by active regions with continual photospheric shearing and converging motions. Here, through high accuracy magnetohydrodynamics simulation, we show how solar eruption is initiated in a single bipolar configuration as driven by first shearing and then converging motions at the bottom surface. Different from many previous simulations, we applied the converging motion without magnetic diffusion, thus it only increases the magnetic gradient across the polarity inversion line but without magnetic flux cancellation. The converging motion at the footpoints of the sheared arcade creates a current sheet in a quasi-static way, and the eruption is triggered by magnetic reconnection of the current sheet, which supports the same scenario as shown in our previous simulation with only shearing motion. With the converging motion, the current sheet is formed at a lower height and has a higher current density than with shearing motion alone, which makes reconnection more effective and eruption stronger. Moreover, the converging motion renders a fast decay rate of the overlying field with height and thus favorable for an eruption. This demonstrate that the converging flow is more efficient to create the current sheet and more favorable for eruption than by solely the shearing flow.

Keywords: Magnetic fields; Magnetohydrodynamics (MHD); **Methods:** numerical; **Sun:** corona; **Sun:** Coronal mass ejections

1 INTRODUCTION

Coronal mass ejections (CMEs) are the most spectacular eruptions on the Sun. They represent a explosive release of free magnetic energy stored in the coronal magnetic field. Due to the line-tied effect of the photosphere, the coronal magnetic field is continuously but slowly dragged at their feet by the photospheric surface motions. Usually, these motions are organized in large scale, such as shearing along the polarity inversion line (PIL), converging towards the PIL, rotation of sunspot, and dispersion of magnetic flux [Chintzoglou et al., 2019; Brown et al., 2003; Min and Chae, 2009; Vemareddy et al., 2012; Vemareddy, 2017; van Driel-Gesztelyi et al., 2003; Lamb et al., 2013]. With these motions (one type of them or their superposition), the coronal magnetic configuration is driven to evolve continually away from the potential field state until a critical point at which no more stable equilibrium can be maintained and an eruption is triggered. Before the onset of the eruption, the Lorentz force dominates and self-equilibrates in the coronal system, that is, the downward magnetic tension force of the overlying, mostly unshredded flux cancels out the outward magnetic pressure force of the low-lying, strongly stressed flux. With initiation of

the eruption, the force balance in the coronal system is catastrophically disrupted and the free magnetic energy is rapidly converted into heating (i.e., flare) and acceleration (i.e., CME) of the plasma.

It remains an open question how solar eruptions are initiated and many theories have been proposed [Forbes et al., 2006; Shibata and Magara, 2011; Chen, 2011; Schmieder et al., 2013; Aulanier, 2014; Janvier et al., 2015], which generally be classified into two categories, the first based on ideal magnetohydrodynamics (MHD) instabilities and the other on resistive process, i.e., magnetic reconnection.

But for eruptions initiated from in most common bipolar configuration on the Sun, most models resort to ideal MHD instabilities that require the pre-existence of a magnetic flux rope (MFR) in the corona before eruption. For example, the kink instability and torus instability of the MFR would initiate an eruption [Kliem and Török, 2006; Török and Kliem, 2005; Fan and Gibson, 2007; Aulanier et al., 2010; Amari et al., 2018]. In the MHD simulations of these models, there needs to be a key phase to transform shear magnetic arcade to MFR before the onset of eruption, such as magnetic cancellation, tether-cutting reconnection, opposite flux emerging [Amari et al., 2000, 2003a,b; Aulanier et al., 2010; Zuccarello et al., 2015; Kusano et al., 2012].

Recently, through ultra-high resolution MHD simulation, Jiang et al. [2021] established a simple and effective mechanism of eruption initiation in bipolar field without the need of a pre-existing MFR. Only through a continual surface shearing motion along the PIL, a vertical current sheet (CS) forms quasi-statically, and once the CS is sufficiently thin, fast magnetic reconnection sets in and instantly initiates and subsequently drives the eruption. This scenario is referred to as the BASIC mechanism (here, BASIC is the abbreviation of the key ingredients as involved in the fundamental mechanism: a Bipolar magnetic Arcade as sheared evolves quasi-statically and forms Internally a Current sheet) [Bian et al., 2022]. In the simulations of the BASIC mechanism, only a shearing flow is applied to the bipolar while the converging flow has not been considered. Actually the latter has been commonly invoked in flux-cancellation model that builds up unstable MFR [van Ballegoijen and Martens, 1989; Amari et al., 2003b; Zuccarello et al., 2015].

In this paper, we are interested in whether the BASIC mechanism can also be effective if there is converging flow to drive the MHD system other than the shearing flow. To address this issue, we perform a 3D MHD simulation by first driving the system with shearing motion and then switching to converging motion driving. The shearing driven phase is stopped well before the CS forms. It is found that the converging motion can still drive the system to form a CS quasi-statically and results in eruption when reconnection sets in, which is essentially the same as when only shearing motion is applied. Compared with shearing motion only, the CS is formed at a lower height and has a higher current density, which makes the reconnection more effective and the eruption stronger. Moreover, the converging motion renders a fast decay rate of the overlying field with height and thus favorable for an eruption. This simulation confirms that the BASIC mechanism also applies with converging flow, and further demonstrates that the converging flow is more efficiently to create the CS and more favorable for eruption than by solely the shearing flow.

This paper is organized as follows. In Sect. 2, we show the MHD model along with the initial and boundary conditions, especially the two types of driven motions. Then the simulation results are presented in Sect. 3. Finally, our conclusions and discussions are given in Sect. 4.

2 NUMERICAL MODEL

Our model is a system of full MHD equations in 3D Cartesian coordinates with both plasma pressure and solar gravity, and is solved by the advanced conservation element and solution element method [Jiang

et al., 2010; Feng et al., 2010; Jiang et al., 2016, 2021]. The basic setup of the model is similar to our previous work [Jiang et al., 2021; Bian et al., 2022], but here we use two types of driven motions, shear and convergence. Our model does not use explicit resistivity in the magnetic induction equation throughout the simulation, but still allows for magnetic reconnection through numerical diffusion when the thickness of the current layer approaches the grid resolution [Jiang et al., 2021]. By this, we achieved a resistivity as small as we can with a given grid resolution.

The calculation volume is a cube box, which is $[-270, 270]$ Mm in the x direction, $[-270, 270]$ Mm in the y direction, and $[0, 540]$ Mm in the z direction. For convenience, we consider $z = 0$ to represent the solar surface (photosphere), since our model is designed to simulate the coronal evolution as driven by the slow (quasi-statically) surface line-tied motions at the footpoints of the coronal magnetic field lines, and the field line footpoints are anchored at the photosphere. The volume is large enough such that the simulation runs can be stopped before the disturbance reaches the side and top boundaries. The full volume is resolved by a block-structured grid with adaptive mesh refinement (AMR) in which the base resolution is $\Delta x = \Delta y = \Delta z = 2.88$ Mm, and the highest resolution is $\Delta = 90$ km, which is used to capture the formation process of the CS and the subsequent reconnection.

The initial magnetic field of the MHD simulation is the potential field obtained by the Green's function method from magnetogram. The photospheric magnetogram is a bipolar field modeled by a combination of two Gaussian functions [Amari et al., 2003a; Jiang et al., 2021],

$$B_z(x, y, 0) = B_0 e^{-x^2/\sigma_x^2} (e^{-(y-y_c)^2/\sigma_y^2} - e^{-(y+y_c)^2/\sigma_y^2}), \quad (1)$$

where $B_0 = 21.3$ G, $\sigma_x = \sigma_y = 28.8$ Mm, and $y_c = 11.5$ Mm. The parameters σ_x and σ_y control the extents of the magnetic flux distribution in the x and y direction, respectively, such a magnetogram is close to two circles (Figure 1A), similar to Aulanier et al. [2010]; Zuccarello et al. [2015], but here it is symmetrical.

The initial background atmosphere in the model is in hydrostatic equilibrium, that is, the gravity of the plasma is balanced with the pressure gradient force. Plasma is set to typical coronal values, with a sound speed of 110 km s^{-1} , the maximum Alfvén speed of 1300 km s^{-1} and the minimum plasma β of 1.3×10^{-2} .

Our MHD simulation is first driven by a rotational flows at each magnetic polarity, which is defined as

$$v_x = \frac{\partial \psi(B_z)}{\partial y}; v_y = \frac{\partial \psi(B_z)}{\partial x}, \quad (2)$$

with ψ given by

$$\psi = v_0 B_z^2 e^{-(B_z^2 - B_{z,\max}^2)/B_{z,\max}^2}, \quad (3)$$

where $B_{z,\max}$ is the maximum value of B_z on the photosphere, and v_0 is a constant for scaling such that the maximum of the surface velocity is 4.4 km s^{-1} , which is close to the magnitude of the typical flow speed on the photosphere ($\sim 1 \text{ km s}^{-1}$). The flow speed is smaller than the sound speed by two orders of magnitude and the local Alfvén speed by three orders, respectively, thus representing a quasi-static stress of the coronal magnetic field. The rotational flow creates magnetic shear along the PIL and does not change

the magnetic flux distribution at the bottom, which is referred to as shearing flow in this paper, and its profile is shown in Figure 1A.

The simulation of CASE IV in our previous work [Bian et al., 2022] was done using the above magnetogram and shearing flow, but the highest grid resolution was 360 km. Through the continual shearing flow along the PIL, the magnetic energy first increases monotonically over a long period of time, during which the kinetic energy remains at a very low level. Then, at a critical point $t = 165$ (the time unit is $\tau = 105$ s, all of the times mentioned in this paper are expressed in the same unit), when the thickness of the CS decreases down to the grid resolution, reconnection begins and triggers an eruption, during which the magnetic energy quickly drops and the kinetic energy rises rapidly to nearly 3% of original potential energy. The scenario of this simulation is the BASIC mechanism.

In order to study whether the BASIC mechanism can also be still effective with converging flow to drive the MHD system other than the shearing flow, we perform this MHD simulation by first driving the system with shearing motion and then switching to converging motion driving, similar to Amari et al. [2003a]; Zuccarello et al. [2015]. The shearing driven phase is stopped at $t = 140$, a typical moment chosen when the system has accumulated a large amount of free energy but the CS has not yet formed, and then the converging driven phase is started. Following Amari et al. [2003a], the converging flow is simply defined as:

$$v_x = 0; v_y = -v_1 B_z(t = 0). \quad (4)$$

where v_1 is also a constant for scaling such that the largest of the velocity is 4.4 km s^{-1} . The converging flow is shown in the Figure 1B. The effect of converging flow on the vertical component of the magnetic field B_z at $t = 165$ is shown in the Figure 1C. The converging flow makes the magnetic flux converge to the PIL, which increases the gradient of the vertical component of the magnetic field B_z along the PIL.

We do not apply magnetic resistivity in the whole computational volume (including the photosphere surface) during the simulation process, so that magnetic cancellation does not occur. The total amount of unsigned flux on the photosphere remains unchanged, while the maximum of the vertical component of the magnetic field B_z becomes larger.

3 RESULTS

Our simulation shows the whole process of the dynamic evolution of the coronal system, including the quasi-static driving process and the subsequent eruption. The evolution of magnetic field lines, electric current and velocity during simulation process can be seen from Figure 2 and Movie. During the shearing driven phase, the evolution of the system is same as our previous work [Bian et al., 2022]. At the end of the shearing driven phase ($t = 140$), a magnetic field configuration with strong shear above the PIL is formed, and the current layer formed is still extremely thick (around 70 grids of highest resolution, see Figure 3), thus far from a CS.

At this point, we stop shearing flow and switch on the converging flow, so that the bottom magnetic flux starts to converge to the PIL. Due to the photospheric line-tied effect, the coronal magnetic field is compressed inwards, and the current layer was squeezed into a narrow vertical CS above the PIL (around 3 grids; see Figures 2C and 3B). The velocity is negligible, and the total kinetic energy is around 0.03% of the magnetic energy before $t = 156$ (Figure 4A), which indicates that the evolution of the system is quasi-static.

Figure 3A shows the structure of the CS in the core region, and the thickness of the CS (at the maximum of current density) is marked in Figure 3B. It can be seen from Figure 3C that the thickness of the CS decreases with time at a rate of the order of kilometer per second, which is consistent with converging flow. The thickness of the CS decreases more rapidly after $t = 152$, about 6.053 km s^{-1} , which is slightly faster than the maximum of converging flow of 4.4 km s^{-1} applied at the bottom boundary. But the evolution of the system is still quasi-static, compared to the Alfvén speed of thousands of kilometers per second.

Figure 4 presents the evolution of energies during the simulation run from initial time to $t = 165$, which includes potential, free and total magnetic energies, as well as kinetic energy. To compute the potential energy of the system, we use equation (7) in Amari et al. [2003a],

$$E_{\text{pot}} = \frac{1}{16\pi^2} \int_{S \times S'} \frac{B_z(x, y, 0)B_z(x', y', 0)}{|\mathbf{r} - \mathbf{r}'|} ds ds'. \quad (5)$$

We extract the vertical component of magnetic field B_z on the bottom surface and remap the AMR grid onto a uniform grid of $[400 \times 400]$ points, and then directly use the Equation 5 to calculate the potential field energy. This method is more time efficient than using the potential field extrapolation method [Bian et al., 2022]. The free magnetic energy is obtained by subtracting the potential energy from the total magnetic energy, which is the volume integral of the magnetic field at a certain moment. From the beginning of the simulation to $t = 140$, during which the system is driven by shearing flow, the potential field energy is constant because the shearing flow does not change the distribution of the bottom surface B_z (Figure 4). At this stage, the total energy increases monotonically, contributed by the free magnetic energy. During the converging phase, i.e., from $t = 140$ to the end of simulation, the total energy continues to increase, and the rate of the energy increase is nearly equal to that of the shearing phase Figure 4A. As the converging flows modified the distribution of B_z at the bottom boundary, the potential field energy showing a slightly decrease, so the increase rate of the free magnetic energy is faster.

During the shearing and converging driven phases, the kinetic energy always keep a very low level, confirming that the evolution of the system is quasi-static. At a critical point ($t = 157$), when the thickness of CS reach grid resolution (Figure 3B), the magnetic reconnection begins and initiates an eruption. The magnetic field energy immediately decreases quickly, meanwhile, the kinetic energy increases rapidly to nearly 10% of original potential energy. The beginning of the eruption can also be clearly shown from the time profiles of the magnetic energy release rate and the kinetic energy increase rate, which both have impulsive increases at the onset of the eruption, as shown in Figure 4B. This eruption initiated conforms to the BASIC mechanism, that is, the reconnection of the quasi-statically formed CS will immediately trigger the eruption.

As the beginning of magnetic reconnection, a plasmoid (i.e., MFR in 3D) originates from the tip of the CS and rises rapidly, leaving behind a cusp structure separating the reconnected, post-flare loops from the unreconnected field, as shown in Figure 2C and Movie. The plasmoid expands rapidly, and meanwhile, an arc-shaped fast magnetosonic shock is formed in front of the plasmoid. Additionally, the turbulence excited by plasmoid-mediated reconnection is also present in our simulations (Figure 2C, at $t \geq 161$), which can actually enhance the reconnection rate. Therefore, this also shows that the simulation in this paper has very high resolution, as plasmoid-mediated reconnection and the resulted turbulence appear only in simulation with sufficiently high resolutions [Jiang et al., 2021; Karpen et al., 2012] with Lundquist number achieving $\geq 10^5$.

The intensity of eruption in this simulation was significantly stronger than CASE IV, both in terms of magnetic energy releasing rate and kinetic energy increasing rate, as shown in Figure 5A. Therefore we compared the two simulations, and results are shown in Figure 5B-D. Figure 5B is the current density distributions of the two simulations along the z axis at the beginning of the eruption. The current density of CASE IV is multiplied by 4, since the highest grid resolution in this simulation is four times that of CASE IV. The CS in this simulation forms at a lower position and has a larger peak current density, which makes the reconnection more efficient and the eruption stronger. Moreover, We also check the effect of the background field on the intensity of eruption by calculating the decay index of the background field at the beginning of these two eruptions. The overlying field B_y actually plays a key role in constraining the erupting flux rope, which is shown in Figure 5C, and the decay index, which is defined as $n = -d \ln(-B_y)/d \ln(z)$, is shown in Figure 5D. Compared with the CASE IV, the decay index is significantly enhanced in a height of 90 to 150 Mm, so that the decay index reaches canonical threshold of 1.5 at lower height, which also favorable for an eruption.

4 CONCLUSION

Our simulations demonstrate that the BASIC mechanism is still effective with photospheric driving motion of jointly shearing and converging flows. At the end of the shearing driven phase, a magnetic field configuration with strong shear above the PIL is formed, and the current layer is still extremely thick. With the progress of the converging driven phase, the degree of magnetic shear above the PIL is further strengthened, and the current layer is compressed to be thinner, finally forming a CS and eventually fast magnetic reconnection sets in and instantly initiates the eruption.

During the whole simulation process, the photospheric unsigned flux remains unchanged, that is, magnetic cancellation does not occur. This constraint excludes the possibility of an MFR forms before the onset of eruption, which is the difference between this simulation and Amari et al. [2003b]; Zuccarello et al. [2015].

Compared with the CASE IV driven by shearing motion only, the converging motion driven used at $t = 140$ advances the formation time of the CS, which is $t = 157$ in this simulation compared to $t = 165$ in CASE IV, that is, it is more effective for forming CS. In addition, the CS is formed in this simulation at a lower height and has a higher current density, which makes the magnetic reconnection more effective and the eruption stronger. Moreover, the converging motion renders a fast decay rate of the overlying field with height and thus favorable for an eruption.

In summary, this simulation confirms that the BASIC mechanism also applies with converging flow, and further demonstrates that the converging flow is more effective to create the CS and more favorable for eruption than by solely the shearing flow.

CONFLICT OF INTEREST STATEMENT

The authors declare that the research was conducted in the absence of any commercial or financial relationships that could be construed as a potential conflict of interest.

AUTHOR CONTRIBUTIONS

XB carried out the simulation and wrote the draft of the manuscript. CJ leads this work and all contribute to the study.

ACKNOWLEDGMENTS

This work is jointly supported by National Natural Science Foundation of China (NSFC 42174200), the Fundamental Research Funds for the Central Universities (HIT.OCEF.2021033), Shenzhen Science and Technology Program (RCJC20210609104422048), and Shenzhen Technology Project JCYJ20190806142609035. The computational work was carried out on TianHe-1(A), National Supercomputer Center in Tianjin, China.

REFERENCES

- Amari, T., Canou, A., Aly, J.-J., Delyon, F., and Alauzet, F. (2018). Magnetic cage and rope as the key for solar eruptions. *Nature* 554, 211–215. doi:10.1038/nature24671
- Amari, T., Luciani, J. F., Aly, J. J., Mikic, Z., and Linker, J. (2003a). Coronal mass ejection: Initiation, magnetic helicity, and flux ropes. i. boundary motion–driven evolution. *The Astrophysical Journal* 585, 1073–1086. doi:10.1086/345501
- Amari, T., Luciani, J. F., Aly, J. J., Mikic, Z., and Linker, J. (2003b). Coronal mass ejection: Initiation, magnetic helicity, and flux ropes. ii. turbulent diffusion–driven evolution. *The Astrophysical Journal* 595, 1231–1250. doi:10.1086/377444
- Amari, T., Luciani, J. F., Mikic, Z., and Linker, J. (2000). A twisted flux rope model for coronal mass ejections and two-ribbon flares. *The Astrophysical Journal* 529, L49–L52. doi:10.1086/312444
- Aulanier, G. (2014). The physical mechanisms that initiate and drive solar eruptions. In *Nature of Prominences and Their Role in Space Weather*. vol. 300, 184–196. doi:10.1017/S1743921313010958
- Aulanier, G., Török, T., Démoulin, P., and DeLuca, E. E. (2010). Formation of torus-unstable flux ropes and electric currents in erupting sigmoids. *The Astrophysical Journal* 708, 314–333. doi:10.1088/0004-637X/708/1/314
- Bian, X., Jiang, C., Feng, X., Zuo, P., Wang, Y., and Wang, X. (2022). Numerical simulation of a fundamental mechanism of solar eruption with a range of magnetic flux distributions. *Astronomy & Astrophysics* 658, A174. doi:10.1051/0004-6361/202141996
- Brown, D., Nightingale, R., Alexander, D., Schrijver, C., Metcalf, T., Shine, R., et al. (2003). Observations of rotating sunspots from trace. *Solar Physics* 216, 79–108. doi:10.1023/A:1026138413791
- Chen, P. F. (2011). Coronal mass ejections: Models and their observational basis. *Living Reviews in Solar Physics* 8. doi:10.12942/lrsp-2011-1
- Chintzoglou, G., Zhang, J., Cheung, M. C. M., and Kazachenko, M. (2019). The origin of major solar activity: Collisional shearing between nonconjugated polarities of multiple bipoles emerging within active regions. *The Astrophysical Journal* 871, 67. doi:10.3847/1538-4357/aaef30
- Fan, Y. and Gibson, S. E. (2007). Onset of coronal mass ejections due to loss of confinement of coronal flux ropes. *The Astrophysical Journal* 668, 1232–1245. doi:10.1086/521335
- Feng, X., Yang, L., Xiang, C., Wu, S. T., Zhou, Y., and Zhong, D. (2010). Three-dimensional solar wind modeling from the sun to earth by a sip-cese mhd model with a six-component grid. *The Astrophysical Journal* 723, 300–319. doi:10.1088/0004-637X/723/1/300
- Forbes, T. G., Linker, J. A., Chen, J., Cid, C., Kóta, J., Lee, M. A., et al. (2006). Cme theory and models: Report of working group d. *Space Science Reviews* 123, 251–302. doi:10.1007/s11214-006-9019-8
- Janvier, M., Aulanier, G., and Démoulin, P. (2015). From coronal observations to mhd simulations, the building blocks for 3d models of solar flares (invited review). *Solar Physics* 290, 3425–3456. doi:10.1007/s11207-015-0710-3

- Jiang, C., Feng, X., Liu, R., Yan, X., Hu, Q., Moore, R. L., et al. (2021). A fundamental mechanism of solar eruption initiation. *Nature Astronomy* 5, 1126–1138. doi:10.1038/s41550-021-01414-z
- Jiang, C., Feng, X., Zhang, J., and Zhong, D. (2010). Amr simulations of magnetohydrodynamic problems by the cese method in curvilinear coordinates. *Solar Physics* 267, 463–491. doi:10.1007/s11207-010-9649-6
- Jiang, C., Wu, S. T., Feng, X., and Hu, Q. (2016). Data-driven magnetohydrodynamic modelling of a flux-emerging active region leading to solar eruption. *Nature Communications* 7, 11522. doi:10.1038/ncomms11522
- Karpen, J. T., Antiochos, S. K., and DeVore, C. R. (2012). The mechanisms for the onset and explosive eruption of coronal mass ejections and eruptive flares. *The Astrophysical Journal* 760, 81. doi:10.1088/0004-637X/760/1/81
- Kliem, B. and Török, T. (2006). Torus instability. *Physical Review Letters* 96, 255002. doi:10.1103/PhysRevLett.96.255002
- Kusano, K., Bamba, Y., Yamamoto, T. T., Iida, Y., Toriumi, S., and Asai, A. (2012). Magnetic field structures triggering solar flares and coronal mass ejections. *The Astrophysical Journal* 760, 31. doi:10.1088/0004-637X/760/1/31
- Lamb, D. A., Howard, T. A., DeForest, C. E., Parnell, C. E., and Welsch, B. T. (2013). Solar magnetic tracking. iv. the death of magnetic features. *The Astrophysical Journal* 774, 127. doi:10.1088/0004-637X/774/2/127
- Min, S. and Chae, J. (2009). The rotating sunspot in ar 10930. *Solar Physics* 258, 203–217. doi:10.1007/s11207-009-9425-7
- Schmieder, B., Démoulin, P., and Aulanier, G. (2013). Solar filament eruptions and their physical role in triggering coronal mass ejections. *Advances in Space Research* 51, 1967–1980. doi:10.1016/j.asr.2012.12.026
- Shibata, K. and Magara, T. (2011). Solar flares: Magnetohydrodynamic processes. *Living Reviews in Solar Physics* 8. doi:10.12942/lrsp-2011-6
- Török, T. and Kliem, B. (2005). Confined and ejective eruptions of kink-unstable flux ropes. *The Astrophysical Journal* 630, L97–L100. doi:10.1086/462412
- van Ballegoijen, A. A. and Martens, P. C. H. (1989). Formation and eruption of solar prominences. *The Astrophysical Journal* 343, 971. doi:10.1086/167766
- van Driel-Gesztelyi, L., Demoulin, P., Mandrini, C. H., Harra, L., and Klimchuk, J. A. (2003). The long-term evolution of ar 7978: The scalings of the coronal plasma parameters with the mean photospheric magnetic field. *The Astrophysical Journal* 586, 579–591. doi:10.1086/367633
- Vemareddy, P. (2017). Successive homologous coronal mass ejections driven by shearing and converging motions in solar active region noaa 12371. *The Astrophysical Journal* 845, 59. doi:10.3847/1538-4357/aa7ff4
- Vemareddy, P., Ambastha, A., and Maurya, R. A. (2012). On the role of rotating sunspots in the activity of solar active region noaa 11158. *The Astrophysical Journal* 761, 60. doi:10.1088/0004-637X/761/1/60
- Zuccarello, F. P., Aulanier, G., and Gilchrist, S. A. (2015). Critical decay index at the onset of solar eruptions. *The Astrophysical Journal* 814, 126. doi:10.1088/0004-637X/814/2/126

FIGURE CAPTIONS

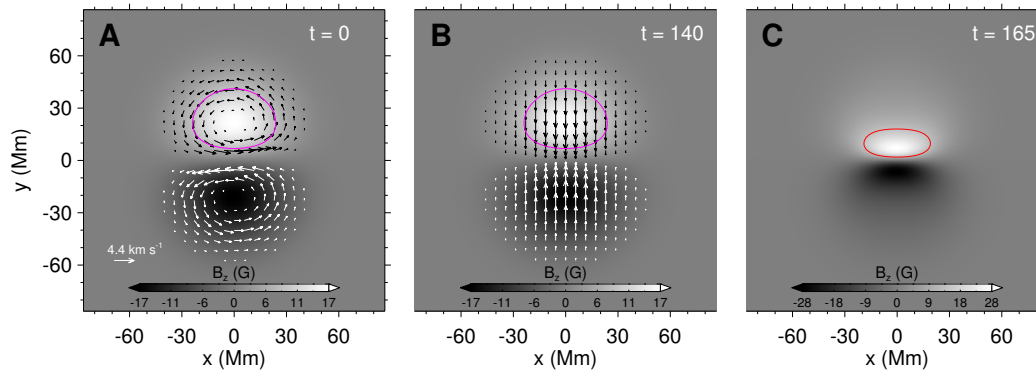


Figure 1. The magnetic flux and velocity of the bottom surface during the simulation. **A**, Magnetic flux distribution and initial surface rotational (shearing) flow (shown by the arrows) at the bottom surface (i.e. $z = 0$). **B**, same as **A**, but the converging flow starting at $t = 140$. **C**, Magnetic flux distribution at time $t = 165$. The magenta and red lines represent the contours of one half of the maximum of magnetic normal component (i.e. $\frac{1}{2}B_{z,\text{max}}$) in each diagram, respectively.

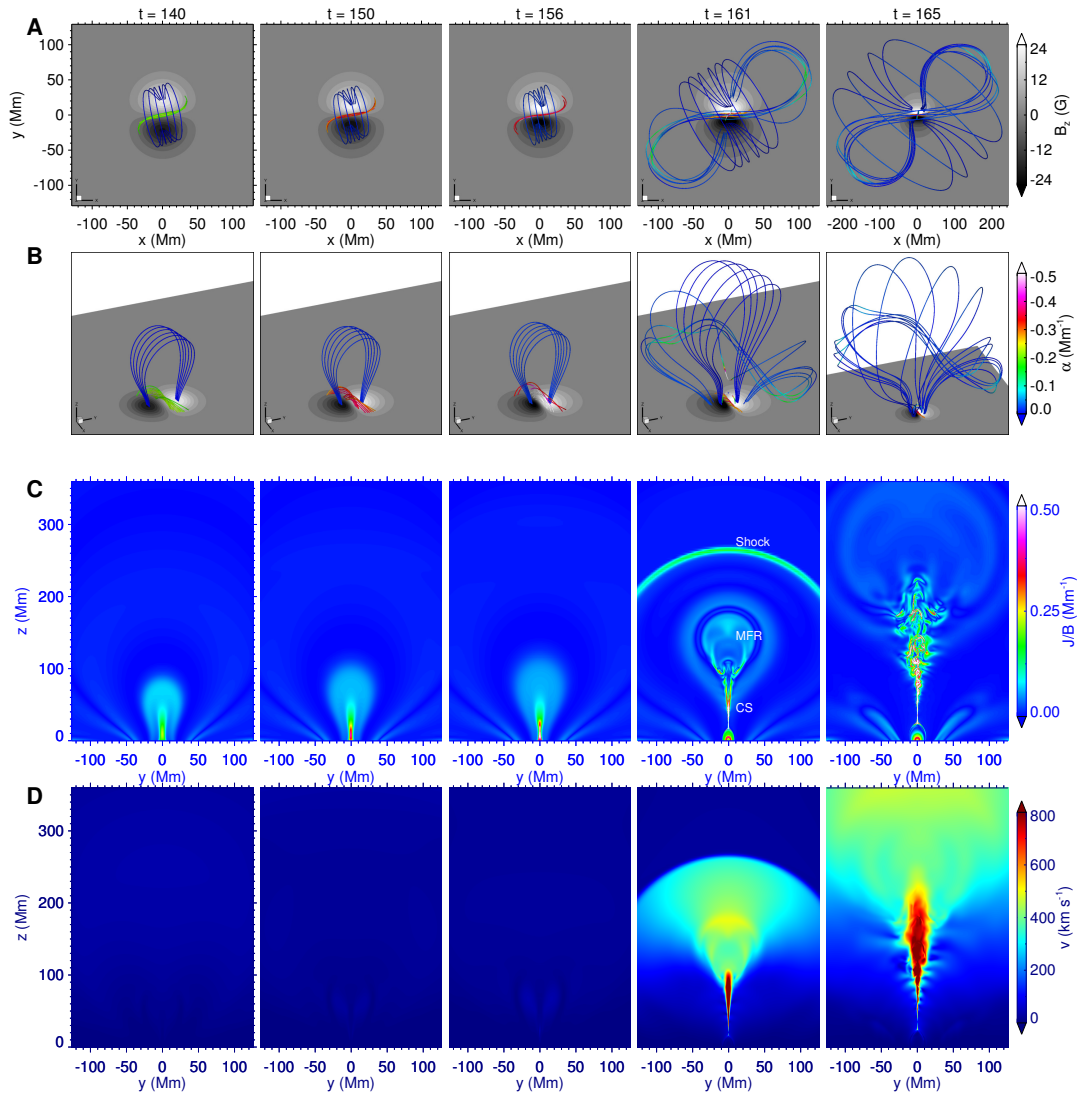


Figure 2. Evolution of magnetic field lines, electric current, and, velocity during simulation process. **A**, Top view of magnetic field lines. The colored thick lines represent magnetic field line and the colors denote the value of nonlinear force-free factor defined as $\alpha = \mathbf{J} \cdot \mathbf{B}/B^2$, which indicates how much the field lines are non-potential. The background is plotted for the vertical magnetic component B_z on the bottom surface. **B**, 3D perspective view of the same field lines shown in panel **A**. The panel with $t = 165$ has a larger range. **C**, Distribution of current density, J , normalized by magnetic field strength, B , on the vertical cross section, that is, the $x = 0$ slice. **D**, Vertical cross section of the velocity. The maximum velocity and Alfvénic Mach number are also denoted.

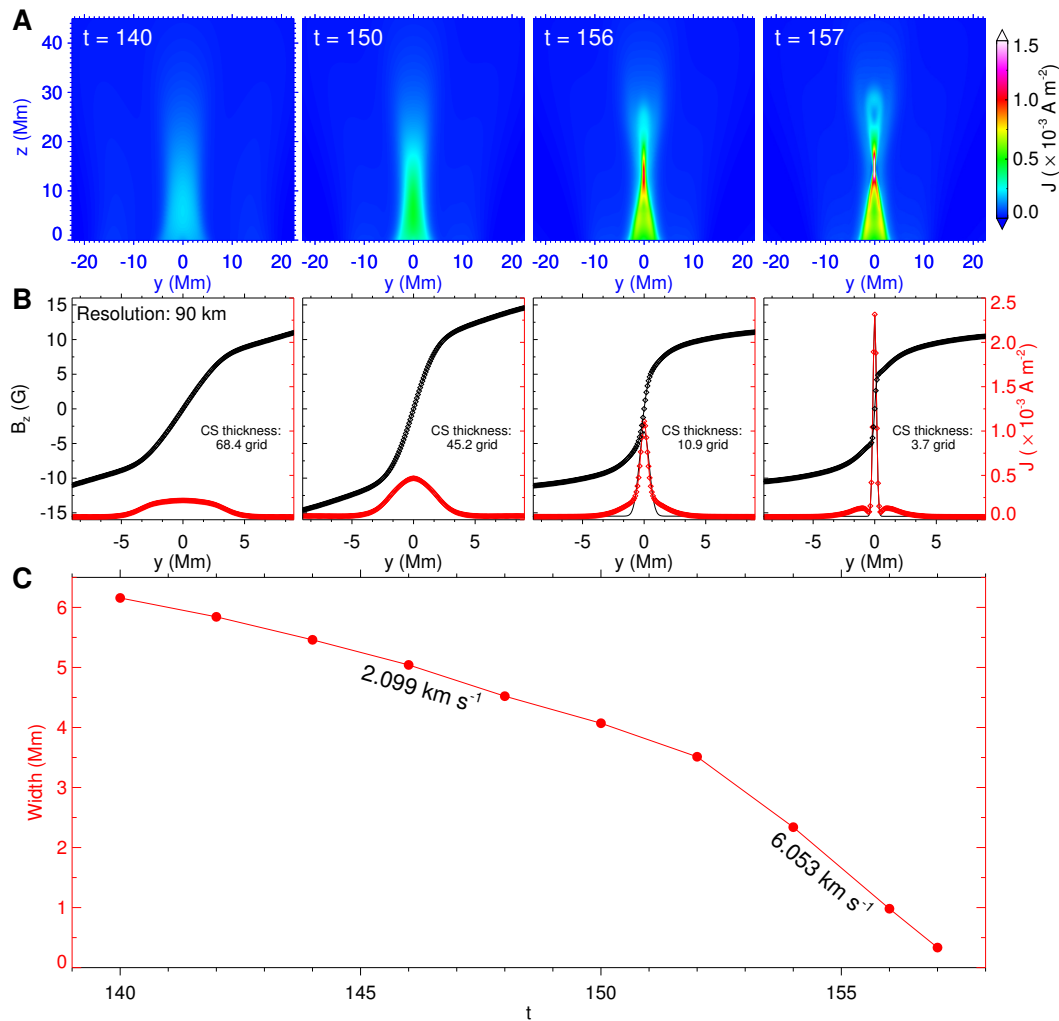


Figure 3. Formation of the CS. **A**, The distribution of current density on the central vertical slice. **B**, One-dimensional profile of the vertical component of magnetic field B_z and current density J along a horizontal line crossing perpendicular to the point with the maximum J . The diamonds denotes values on the grid nodes. The thickness of CS is denoted, which is defined by the FWHM of a Gauss function fitting (the thin black curve) of the profile of current density. **C**, Thickness evolution of the CS during converging driven process as shown in **B**. The velocity at which the thickness of the CS changes is also given. The boundary between these two velocities is $t = 152$.

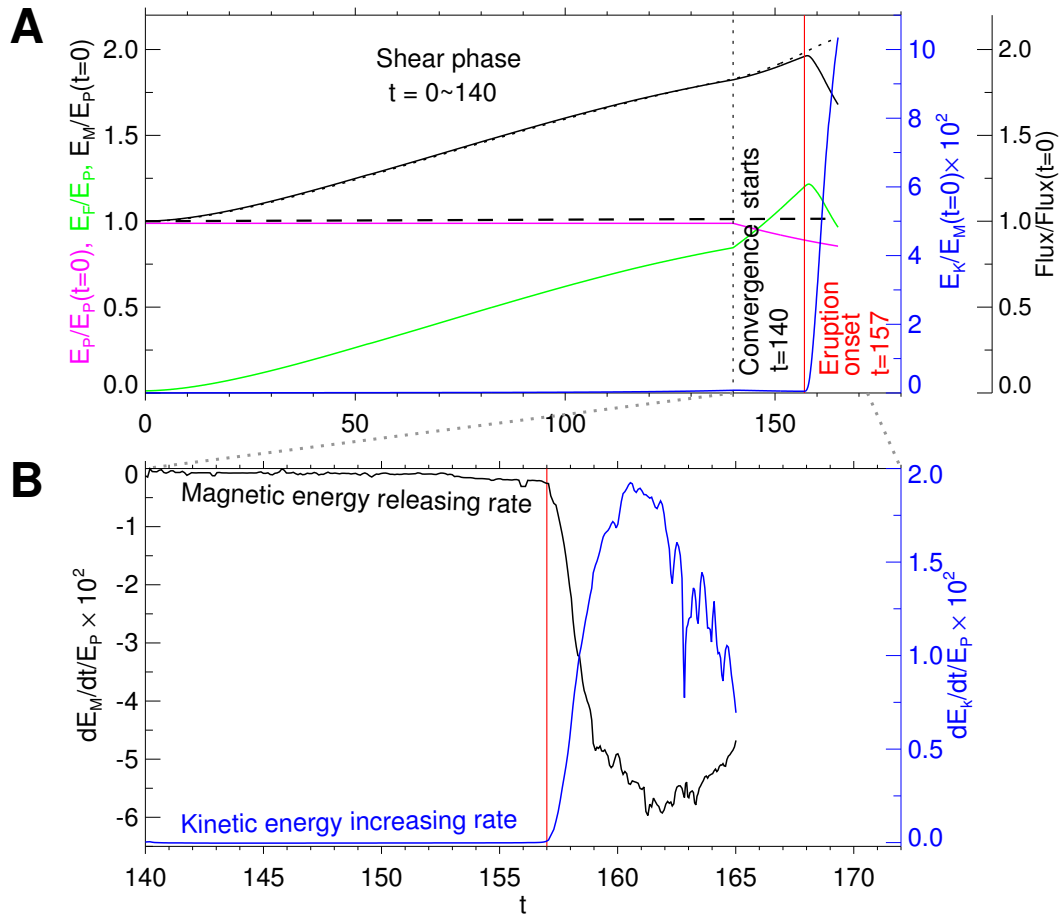


Figure 4. Temporal evolution of magnetic energies, kinetic energy and magnetic flux in the simulation. **A**, Evolution of total magnetic energy E_M (black), free magnetic energy E_F (green), potential magnetic energy E_P (magenta), kinetic energy E_K (blue line), and magnetic flux (black dashed line). The dotted curve represents the energy injected into the full volume from the bottom boundary through the surface flow. Vertical black dotted line denotes the beginning of the converging flow and vertical red line denotes the transition time from pre-eruption to eruption. **B**, Magnetic energy releasing rate (black line) and the kinetic energy increasing rate (blue line).

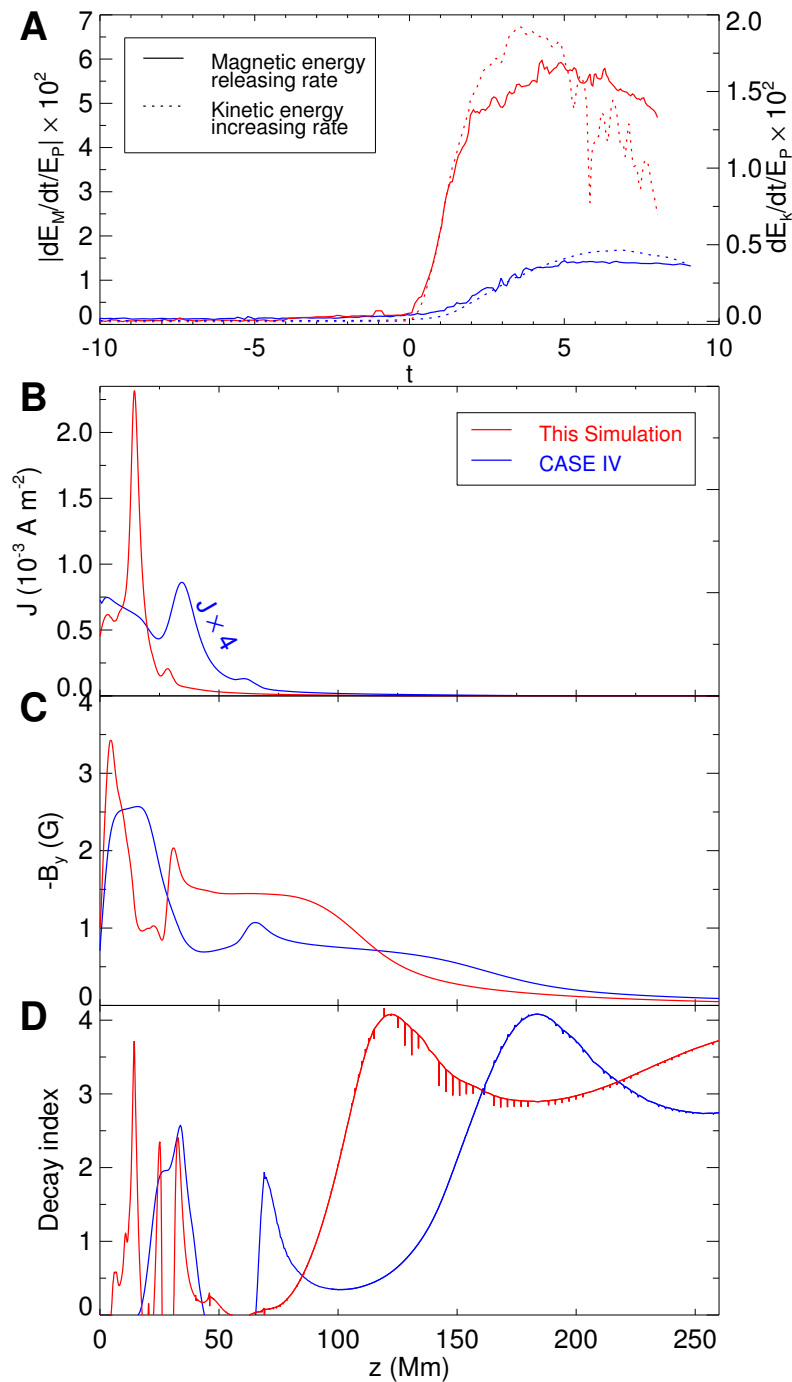


Figure 5. Intensity of eruption, current density, magnetic field and decay index for this eruption and CASE IV. **A**, Magnetic energy releasing rate (solid line) and the kinetic energy increasing rate (dotted line). The timescale is shifted so that the $t = 0$ represents the eruption onset. Red and blue curves represent the this simulation and CASE IV, respectively. From top to bottom are shown for **(B)** current density, **(C)** magnetic field component B_y , and **(D)** decay index of B_y , respectively, along z axis, on the eruption onset (this simulation $t = 157$ and CASE IV $t = 165$).

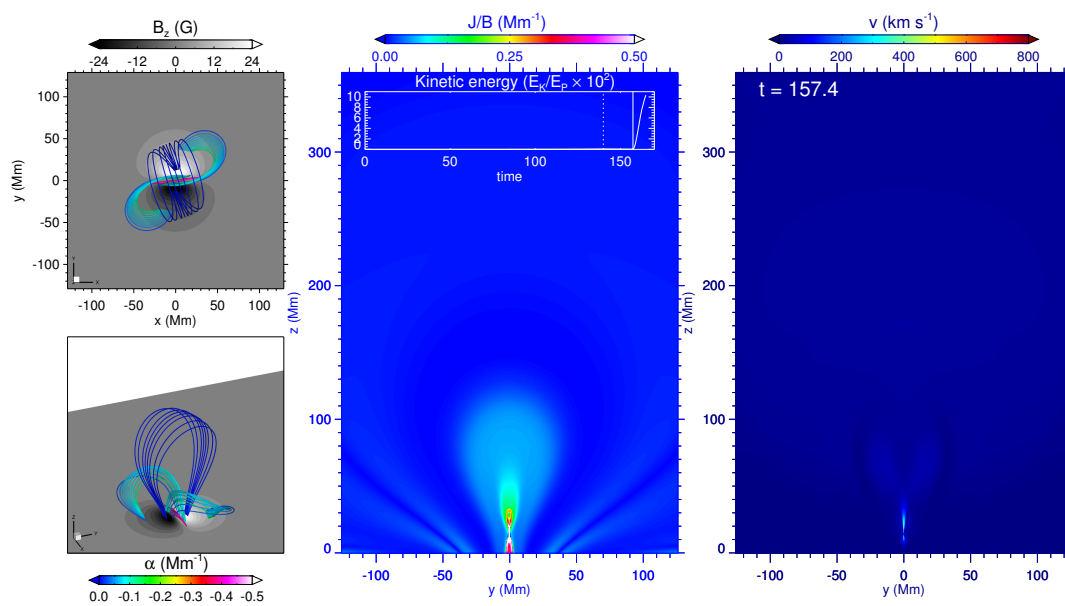


Figure 6. Screenshot of an animation of the Figure 2 in the whole simulation process from the initial time to $t = 165$. This figure is available as an animation.